Catalysis Science & Technology

Direct Synthesis of Furfuryl Alcohol from Furfural: Catalytic Performance of Monometallic and Bimetallic Mo and Ru Phosphides

Journal:	*Catalysis Science & Technology*
Manuscript ID	CY-ART-04-2019-000705.R1
Article Type:	Paper
Date Submitted by the Author:	04-Jun-2019
Complete List of Authors:	Bonita, Yolanda; University of Notre Dame Jain, Varsha; Mississippi State University, Dave C. Swalm School of Chemical Engineering Geng, Feiyang; University of Notre Dame O'Connell, Timothy; University of Notre Dame Wilson, Woodrow; Mississippi State University, Dave C. Swalm School of Chemical Engineering Rai, Neeraj; Mississippi State University, Dave C. Swalm School of Chemical Engineering Hicks, Jason; University of Notre Dame

ARTICLE

Direct Synthesis of Furfuryl Alcohol from Furfural: Catalytic Performance of Monometallic and Bimetallic Mo and Ru Phosphides

Received 00th January 20xx,
Accepted 00th January 20xx

DOI: 10.1039/x0xx00000x

Yolanda Bonita[a], Varsha Jain[b], Feiyang Geng[a], Timothy P. O'Connell[a], Woodrow N. Wilson[b], Neeraj Rai[b], and Jason C. Hicks[a]*

The catalytic properties of monometallic and bimetallic Ru and Mo phosphides were evaluated for their ability to selectively hydrogenate furfural to furfuryl alcohol. Monometallic MoP showed high selectivity (98%) towards furfuryl alcohol, while RuP and Ru_2P exhibited lower selectivity at comparable conversion. Bimetallic promotional effects were observed with $Ru_{1.0}Mo_{1.0}P$, as the pseudo-first order reaction rate constant for furfural hydrogenation to furfuryl alcohol, k_1, was at least 5x higher than MoP, RuP, and Ru_2P, while maintaining a 99% selectivity. Composition-directed catalytic studies of $Ru_xMo_{2-x}P$ ($0.8 < x < 1.2$) provided evidence that Ru rich compositions positively influence k_1, but not the selectivity. The rate constant ratio (k_1/k_2+k_3) for furfuryl alcohol production compared to methyl furan (k_2) and tetrahyrofurfuryl alcohol (k_3) followed the trend of $Ru_{1.0}Mo_{1.0}P > Ru_{1.2}Mo_{0.8}P > MoP > Ru_{0.8}Mo_{1.2}P > RuP > Ru_2P$. Diffuse reflectance infrared Fourier transform spectroscopy (DRIFTS) was used to examine the configuration of adsorbed furfural on the synthesized catalysts, but the results were inconclusive and no correlation could be found with the selectivity due to the IR inactive surface modes possible with furfural adsorption. However, gas phase density functional theory calculations suggested the $x = 1$ material in $Ru_xMo_{2-x}P$ ($0.8 < x < 1.2$) had the most favorable furfural adsorption energy. Experimentally, we also observed that the solvent greatly influenced both the conversion and selectivity, where isopropanol provided the highest selectivities to furfuryl alcohol. Finally, recycling experiments showed a 12% decrease in k_1 after 3 cycles without any regeneration, but the activity could be fully recovered through a re-reduction step.

Introduction

Furfuryl alcohol (FOL) is an important chemical intermediate with a variety of applications in resins, lubricants, fragrances, flavorings, and lysine production.[1-4] In current furfuryl alcohol production, Cu-chromite ($CuCr_2O_4$) is used as a catalyst to selectively hydrogenate furfural (FAL), a platform molecule that is also derived from lignocellulosic biomass.[5, 6] Although Cu-chromite achieves high selectivity to FOL (>99%) at complete conversion, two primary issues have been identified with this catalytic system: (1) environmental concerns exist with the disposal of spent Cu-chromite catalysts,[5] and (2) Cu-chromite suffers from rapid deactivation due to coke formation or via a change in the Cu oxidation state during reaction.[5, 7, 8]

A variety of alternative Cu-based catalysts have been studied in significant detail, including Cu/C, Cu/ZnO, Cu-Ni, Cu-Co, and Cu-Fe.[9-14] In bimetallic Cu-Fe and Cu-Ni, structural and electronic effects from well-distributed metal atoms or charge transfer between the metals contributed to variations in the catalytic performance for FAL hydrogenation.[9, 10] As a result, a shift in the product distribution was observed where methylfuran (MF) was the dominant product.[9, 10] Noble metal-based catalysts such as Pt, Rh, Pd, and Ru have also been reported as highly active catalysts for FAL hydrogenation.[15] Nevertheless, the main hydrogenation product observed was tetrahydrofurfuryl alcohol (THFA), which was formed via FOL ring hydrogenation. Efforts to tune the selectivity of noble metal catalysts have included pairing the noble metal with a less reactive metal such as Sn, where the incorporation of Sn can either improve the FAL selectivity when paired with Ru or increase the reactivity when paired with Pt.[16, 17] Other metals such as Mo, Mn, and Fe have also been shown to enhance the selectivity to FAL in Pt-based materials.[18]

Noble metal based phosphides such as Ru_xP, Rh_2P, and Pd_3P were able to deoxygenate biomass-derived molecules,[19-21] with MoP and Ni_2P as potential catalysts for vapor phase furfural hydrogenation to form methyl furan.[22] We have recently reported the low temperature hydrogenation ability of noble metal-based bimetallic $Ru_{1.0}Mo_{1.0}P$ for hydrogenation of various aromatic functionalities such as benzaldehyde to benzyl alcohol.[23, 24] The Lewis acidic nature of $Ru_{1.0}Mo_{1.0}P$ was responsible for the reduction of the aldehyde and is a reasonable catalyst for the selective production of FOL from FAL.[24]

[a] Department of Chemical and Biomolecular Engineering, University of Notre Dame, Notre Dame, Indiana 46556, United States. E-mail: jhicks3@nd.edu
[b] Dave C. Swalm School of Chemical Engineering and Center for Advanced Vehicular Systems, Mississippi State University, Mississippi State, Mississippi 39762, United States

Electronic Supplementary Information (ESI) available: [details of any supplementary information available should be included here]. See DOI: 10.1039/x0xx00000x

Herein, we report a detailed comparison of monometallic MoP, Mo_3P, RuP, Ru_2P phosphides and bimetallic $Ru_xMo_{2-x}P$ phosphides for FAL hydrogenation. A series of experiments and simulations were used to determine the following: (1) if transition metal phosphides were capable of performing selective hydrogenation of FAL to FOL, (2) if an enhancement in catalytic activity and selectivity is observed with bimetallic materials, and (3) the catalytic consequences of changing the metal ratio in $Ru_xMo_{2-x}P$. We close this manuscript with recycle studies of high performing bimetallic catalysts.

Experimental

Materials

Citric acid monohydrate (Amresco, 99%), $(NH_4)_6Mo_7O_{24}{\cdot}4H_2O$ (Alfa Aesar, 99%), $RuCl_3{\cdot}xH_2O$ (Oakwood Chemicals, 90%), $(NH_4)_2HPO_4$ (Amresco, 98.6%), furfural (Sigma Aldrich, 99.5%), furfuryl alcohol (TCI Chemicals), 2-methyl furan (TCI Chemicals, 99%), tetrahydrofurfuryl alcohol (Alfa Aesar, 99%), 2-propanol (J.T. Baker, 99%), 5% Ru/Al_2O_3 (Riogen).

All of the gases are purchased from Airgas: H_2 (99.999%), N_2 (99.999%), 1%O_2/He, 30%CO/He, 2%NH_3/He.

Material synthesis

All materials were synthesized using a temperature programmed reduction (TPR) method described in our previous work and included in the supporting information.[23, 25-27]

Catalyst characterization

The synthesized materials were characterized using various methods. A Bruker powder x-ray diffractometer (XRD) with a Cu-Kα source was used to confirm the crystal structures of the materials. Rietveld refinement was performed using FullProf Suite software. A Si (111) standard was added, and the corresponding peak was shifted to 28.44° 2θ. The Brunauer-Emmett-Teller (BET) surface area was measured with a Quantachrome Nova 2200e with N_2 at 77 K. A Micromeritics Chemisorb 2750 unit equipped with a thermal conductivity detector (TCD) was used to quantify the CO-accessible sites. For CO-pulse chemisorption experiments, the samples were pretreated under 20 mL/min of H_2 flow at 400°C with a 10°C/min ramp rate for 2 h followed by 20 mL/min of He flow at the same temperature for 1.5 h and 20 mL/min of H_2 flow at 100°C for 1 h to prevent polycarbonyl formation.[28] The CO-pulse was performed at 35°C with 0.1 mL injections of 30% CO in He. The amount of CO chemisorbed was quantified using an external calibration curve. The desorption was performed using a 10°C/min ramp rate to a final temperature of 450°C. Elemental analysis was done with a Perkin Elmer Optima 8000 Inductively Coupled Plasma (ICP) – Optical Emission Spectroscopy (OES) system and quantified using an external calibration.

X-Ray Photoelectron Spectroscopy (XPS) was used to determine the binding energies of the various catalysts. All sample preparations occurred in a N_2 glove box, and the exposure to air during sample transfer was minimized. Elemental Ni powder was physically mixed into the sample as a standard where the Ni $2p_{3/2}$ peak was shifted to 852.60 eV. Asymmetric peak fitting was applied in the deconvolution of XP spectra peaks.[29-31] The XP spectra in the Mo 3d region was deconvoluted into the reduced Mo $3d_{5/2}$ and $3d_{3/2}$ pair. The contribution from the oxidized species can be observed in the satellite peak that was deconvoluted into the oxidized Mo $3d_{5/2}$ and $3d_{3/2}$ pair. The low amount of oxidized species observed was attributed to the brief exposure to air during sample transfer or possibly an oxidized layer that formed during passivation. The P 2p region was deconvoluted into the reduced $2p_{3/2}$ and $2p_{1/2}$ doublet and the oxidized $2p_{3/2}$ and $2p_{1/2}$ doublet at higher binding energies. The Ru 3p region was deconvoluted into the reduced $3p_{3/2}$ and $3p_{1/2}$ doublet as well as its oxidized contributions. The Ru 3p region was used to determine the surface composition of the materials since the Ru 3d region overlaps with the C 1s peak.

X-ray absorption spectroscopy (XAS) experiments were performed at Argonne National Laboratory in the Advanced Photon Source sector 10 Insertion Device (ID) line of the Material Research Collaborative Access Team (MRCAT). Boron nitride was used to dilute the samples to obtain a sufficient signal. Approximately 10 mg of the mixture was pressed into a pellet in the sample holder. The sample was placed inside a sealed pretreatment cell, and the samples were pretreated at 450 °C under 4% of H_2 in He for 1 hr. After the cell was cooled down, the cell was sealed and placed for analysis. The measurements were obtained under transmission mode with a 10^5 photon flux per second. WinXAS 3.1 was used to analyze the data.

A Bruker Vertex 70 Fourier transform infrared (FTIR) spectrometer equipped with a Harrick Praying Mantis diffuse reflectance high temperature reaction cell (ZnSe windows) accessory was used to study the interaction of furfural with the catalyst surface. In a typical experiment, the catalyst sample (20 mg) was loaded in the sample cup and pretreated with 30 mL/min of H_2 at 400°C for 2 h followed by 30 mL/min of N_2 at 400°C for 1 hour. After the pretreatment, the sample was cooled down to room temperature, and a background measurement was performed. Furfural was loaded into a glass bubbler with 30 mL of N_2 flow used as the carrier gas to saturate the sample for 30 mins at room temperature. The saturated samples were then purged with N_2 for 30 mins. The IR spectra were recorded over 1000 scans with a 1 cm^{-1} resolution with a liquid N_2 cooled mercury cadmium telluride (MCT) detector.

Catalyst testing

The catalytic testing was performed in a 300 mL Parr batch reactor. Based on the CO chemisorption experiments, the reactor was loaded with the same amount of catalyst in each experiment (0.45 µmol of CO sites for each catalyst). The reaction media consisted of 40 mL of 0.1 M FAL in isopropanol with dioxane added as an internal standard unless otherwise specified. The reactor was charged with H_2 to the pressure of interest. Using a 1/16" sampler tube installed inside the reactor, 250 µL samples were taken at various times during the reaction. The line was flushed between each sampling in order to prevent any cross contamination with previous sampling times. The reaction results were analyzed using gas chromatography – mass spectrometry (GCMS, Agilent 5975-7890) and quantified with an external calibration curve created for each reactant and product. The carbon balance for all points was >95%. The conversion and selectivity were calculated according to

Equation (1) and (2) respectively where X_{FAL} is the FAL conversion, S_{FOL} is selectivity to FOL, and C_j is the concentration of the species, j.

$$X_{FAL} = 1 - \frac{C_{FAL,out}}{C_{FAL,in}} \quad (1)$$

$$S_{FOL} = \frac{C_{FOL}}{C_{FOL} + C_{MF} + C_{THFA}} \quad (2)$$

The conversion over time was fitted into a pseudo-1st order batch reactor equation (Equation 4) that was obtained from Equation 3 to extract the reaction rate constant, k_1, for furfural hydrogenation to furfuryl alcohol.

$$\frac{dC_{FAL}}{dt} = -k_1 C_{FAL} \quad (3)$$

$$-\ln(1 - X_{FAL}) = k_1 t \quad (4)$$

Subsequent reactions with 0.10 M furfuryl alcohol as the substrate were performed to extract the rate constant of MF and tetrahydrofurfuryl alcohol (THFA), denoted as k_2 and k_3, respectively. Equation 5 was derived for parallel 1st order reactions in a batch reactor. Accordingly, a plot of ln (1-X_{FOL}) against time resulted in a slope of $k_2 + k_3$.

$$C_{FOL} = C_{FAL,in}\exp(-(k_2 + k_3)t) \quad (5)$$

The time-dependent C_{MF} and C_{THFA} values in Equation 6 and 7 were then derived. The ratio between C_{MF} and C_{THFA} resulted in Equation 8, which was plotted to obtain k_2/k_3. Using these equations, k_2 and k_3 were determined.

$$C_{MF} = \frac{k_2 C_{FOL,in}}{k_2 + k_3}(1 - \exp(-(k_2 + k_3)t)) \quad (6)$$

$$C_{THFA} = \frac{k_3 C_{FOL,in}}{k_2 + k_3}(1 - \exp(-(k_2 + k_3)t)) \quad (7)$$

$$C_{MF} = \frac{k_2}{k_3} C_{THFA} \quad (8)$$

Computational details

We performed plane wave periodic density functional theory (DFT)[32, 33] calculations using Vienna *ab initio* simulation package (VASP.5.4.4).[34-37] We used the optB88-vdW functional, which accounts for nonlocal, long-range van der Waals interactions.[38, 39] The core electrons are described with the projector augmented wave (PAW) method[40] to solve the Kohn-Sham equations.[41, 42] The energy cut-off was taken as 450 eV to ensure high precision. Total energies were calculated using a first-order Methfessel–Paxton smearing function with a width of 0.1 eV, and the total energy was extrapolated to 0 K.[43] Optimizations were carried out until the net forces acting on atoms were smaller than 0.03 eV $Å^{-1}$, using a total energy convergence of $1x10^{-5}$ eV. The calculations were carried out with spin polarization. For the integration of the Brillouin zone (BZ), we used a Γ-point sampling in all calculations.[44] The partial charges on various species were derived using a Bader charge analysis.[45-48]

Crystal structures of three $Ru_xMo_{2-x}P$ catalysts were optimized in three-dimensional periodic boundary conditions based on the cell parameters determined via XRD patterns of these catalysts. Optimized unit cell parameters in these catalysts showed a deviation of ≤ 1 % in comparison with those experimentally determined (Table S1). Using these optimized cell parameters, the model phosphide surface was constructed by implementing the standard slab approach, in which a slab of finite thickness was cut out of the $Ru_xMo_{2-x}P$ crystal at the (112) plane to expose an atomic layer that has all three types of atoms in each catalytic surface. We applied the same approach to the (210) plane for comparison between the two surfaces. The number of phosphorus atoms was maintained constant (60 atoms) for all the calculations, whereas the number of Ru and Mo atoms was governed by the stoichiometry.

The slab used for simulations consists of three layers in $Ru_xMo_{2-x}P$ with a supercell size P (2 X 2) with a 15 Å thick vacuum layer in the z-direction (perpendicular to the surface) to minimize interactions between neighboring image slabs. For all calculations, the bottom most layer was fixed to represent the corresponding crystal structure obtained from DFT, whereas all other atoms were allowed to relax.

The adsorption energies (denoted as E_{AD}) were calculated according to Eqn. (9), wherein $E_{ADSORBATE+SURFACE}$ is defined as the total energy of species adsorbed on the surface; $E_{SURFACE}$ is defined the total energy of surface; and $E_{ADSORBATE}$ is defined as the energy of the adsorbed species on the surface in the gas phase.

$$E_{AD} = E_{ADSORBATE+SURFACE} - E_{SURFACE} - E_{ADSORBATE} \quad (9)$$

Result and Discussion

Catalytic evaluation of monometallic phosphides

Four unsupported monometallic phosphides MoP, Mo_3P, RuP, and Ru_2P were synthesized using the TPR method described in detail in the supporting information. The crystal structures were confirmed using XRD (Figure S1 and Figure S2).

Table 1 summarizes the textural properties of all the phosphide catalysts used in this study as well as results from CO titrations (N_{CO}). The S_{BET} was obtained using N_2 physisorption, and the values ranged from 6.1 m^2/g – 12 m^2/g for all materials except for MoP (32 m^2/g), which are similar to other reports.[49-51] The S_{BET} of Mo_3P was lower than MoP due to higher reduction temperature needed to synthesize Mo_3P (800°C). It is possible to vary the amount of citric acid added during synthesis to increase the surface area of the resulting materials.[52] Supporting the phosphides can improve the surface area; however, multiple phases can be formed, and the various phosphide phases may add complexity to the evaluation of their catalytic performance.[53, 54] CO-pulse chemisorption was used to quantify the number of CO adsorption sites for each of the phosphide catalysts. The CO-titration results provided similar values ranging between 20-28 µmol/g on all materials, and these values were used to standardize the experiments as well as normalize the reaction rates in some cases.

Table 1. Textural properties of Mo-based and Ru-based

Catalysts	S_{BET} (m^2/g)	N_{CO} (µmol/g)
MoP	32	28
Mo_3P	6.1	25
RuP	12	23

Ru_2P	10	24
$Ru_{0.8}Mo_{1.2}P$	9.2	21
$Ru_{1.0}Mo_{1.0}P$	7.2	20
$Ru_{1.2}Mo_{0.8}P$	11	25

Scheme 1 represents the reaction pathways observed in this study. In the first hydrogenation step, FAL is converted into FOL with a rate constant denoted as k_1. To measure this rate constant, the monometallic catalysts were tested in a batch reactor with 0.10 M FAL in isopropanol at 100°C and 4.2 MPa. Using the CO chemisorption values, the catalyst loading in each experiment was maintained at 0.45 µmol of CO accessible sites for all experiments based on the invariance observed between the consumption rate of furfural with respect to the catalyst amount (Figure S3) and prior literature suggesting CO titrated sites as the active sites for FAL hydrogenation.[5, 16] Samples were taken throughout the reaction, and the conversion was plotted according to Equation 4 to obtain a pseudo-1st order rate constant, k_1.

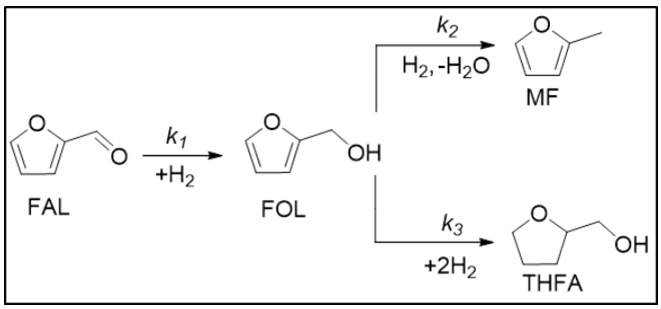

Scheme 1. Reaction pathway of FAL hydrogenation to produce FOL, MF, and THFA

Several reaction mechanisms based on a Langmuir-Hinshelwood model have been proposed for FAL hydrogenation involving adsorption of both H_2 and FAL.[11, 55-58] From these mechanisms, several rate laws has been derived in the literatures.[11, 56, 57] In each of these cases, dependence on both H_2 and FAL concentrations complicate the rate measurements.

To simplify the kinetic expression, the reaction was operated at the appropriate pressure such that the rate depended only on FAL and not H_2. To confirm that the operating H_2 pressure was in the 0th order region, several experiments were performed at 100°C with different partial pressures of H_2 while keeping the total pressure of 4.2 MPa using N_2 as the balancing gas. The results are plotted in Figure S4 as -ln (1-X) against reaction time, where X is the FAL conversion. The reaction constant, k_1, was obtained from the slope of the plot in Figure S4 for 2.1 MPa, 3.4 MPa, 3.8 MPa, and 4.2 MPa H_2 partial pressure. The linear dependency between -ln (1-X) and reaction time observed in the plot implied a pseudo-1st order dependency in FAL concentration could be assumed. Moreover, the kinetic profiles and k_1 were statistically invariant according to the Dixon q-test (Equation S1) in experiments between 3.4 – 4.2 MPa H_2 partial pressure, which provided a suitable kinetic region to compare catalytic materials.[59]

In addition to the H_2 pressure study, the initial concentration of FAL was varied to confirm the pseudo-1st order trend initially observed. With a 4.2 MPa H_2 pressure, five initial concentrations of FAL in IPA (0.10M, 0.15M, 0.18M, and 0.25 M) were studied in a batch reactor at 100°C with real-time sampling of the reaction progress. The reaction results are plotted as -ln (1-X) versus time in Figure S5 for all initial FAL concentrations. The linear trend observed in the plot further indicated pseudo-1st order behavior in FAL for all initial concentrations. Moreover, the k-values were extracted from the slopes to yield k_1 of 0.176 h^{-1}, 0.177 h^{-1}, 0.171 h^{-1}, and 0.174 h^{-1} for initial concentration of 0.10 M, 0.15 M, 0.18 M, and 0.25 M, respectively. At higher FAL concentration (i.e., 0.50 M), the solubility of H_2 decreases and new reaction conditions to satisfy the pseudo-1st order model with excess H_2 in solution are requried.[60] Therefore, to fulfill the pseudo-1st order assumptions, an initial concentration of 0.10 M for FAL is used throughout the experiments. At lower concentrations (0.01 M – 0.05 M), lower than unity order dependency was observed as shown in other reports for FAL hydrogenation over a Pt/C catalyst.[55] The rate expression can therefore be simplified to Equation 3, with k_1 representing the lumped, pseudo-1st order reaction rate constant.

Background experiments were also performed to quantify the contribution of H_2 transfer from isopropanol (solvent). After 24 h of reaction time at 4.2 MPa of N_2 pressure for proper comparison, the furfural conversion was 1.1% with only isopropanol as the H_2 source. Therefore, these contributions were considered negligible in this study. After linearization of Equation 10, the various catalysts were studied and compared (Figure 1). The rate constant, k_1, was measured as 0.030 h^{-1}, 0.027 h^{-1}, and 0.029 h^{-1} for RuP, Ru_2P, and MoP, respectively. These rate constants were similar in magnitude for all monometallic materials. Mo_3P was also tested for this reaction, but it was inactive at temperatures tested below 125°C, which is likely due to unfavorable adsorption of the reactant as also noted by Xiao et al.[61] At much higher temperatures (>300°C), however, Mo_3P was active with ~80% selectivity to 2-(isopropoxy)methyl furan from the etherification reaction between FAL and isopropanol. This result is a possible indication of the weak (or lack of) Brønsted acidity of the phosphides, resulting in the production of the ether product.[24, 62-64]

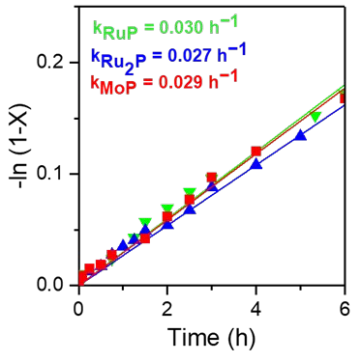

Figure 1. The difference in rate constant k_1 between monometallic RuP (green – R^2 = 0.976), Ru_2P (blue – R^2 = 0.984), and MoP (red – R^2 = 0.987)

All active catalysts also showed a high selectivity to FOL production. At a conversion of 15%, the selectivity towards FOL was 98 ± 0.8% for MoP, while the selectivity decreased slightly to 97 ± 1.2% and 94 ± 1.3% for RuP and Ru_2P, respectively, with MF observed as the other by-product. It was apparent that MoP showed the highest selectivity towards FOL, while the highest rate constant was observed with RuP.

Subsequently, FOL was used as a reactant to determine k_2 and k_3, which correspond to rate constants to produce MF and THFA, respectively (Scheme 1). The constants were determined with batch reaction experiments using 0.10 M FOL in isopropanol as a reactant. Equation 5 and Equation 8 were used to extract k_2 and k_3 values simultaneously. These values were then used to model the concentration of FOL, MF, and THFA with all active monometallic catalysts. The model was plotted with the raw data for MoP, RuP, and Ru_2P in Figure 2a-c. From these plots, it could be seen that the model fits the raw well. The k-values are compiled in Table S3 for comparison. The rate constants for MF formation (k_2) were 0.0035 h^{-1}, 0.0013 h^{-1}, and 0.0002 h^{-1} for MoP, RuP, and Ru_2P, respectively. The rate constants for THFA (k_3) were 0.0185 h^{-1} and 0.1752 h^{-1} for RuP and Ru_2P, respectively, where no THFA was observed with MoP. From these measurements, Ru_2P displayed the highest k_3 value, which suggested high preference for THFA production. High selectivities to THFA from FOL hydrogenation have also been observed in the literature with Ru/TiO_2 along with other noble metal catalysts (Pd, Rh) and Ni boride catalysts.[65, 66] It has been noted that phosphides and borides share a similar metal-metalloid interaction (M-B and M-P) as well as B-B and P-P interactions.[67] It is plausible that the formation of THFA observed in both phosphides and borides is due to the existence of similar sites (i.e., $M^{\delta+}$ or $P^{\delta-}$).[15]

The binding energy shifts of the monometallic Ru and Mo phosphides were measured with XPS to provide the relative oxidation of the materials (Table S4). The Mo $3d_{5/2}$ binding energy shift was determined as 228.2 eV and 227.5 eV for MoP and Mo_3P, which were more oxidized when compared to Mo^0 (i.e. 226.7 eV). Conversely, the P $2p_{3/2}$ binding energy shift was found to be 129.5 eV and 129.1 eV for MoP and Mo_3P, respectively. These values were in the range of negatively charged P (i.e. 130.0 – 130.9 eV).[68] A similar observation was also observed with the monometallic Ru phosphides. The binding energy shift of Ru $3p_{3/2}$ in Ru_2P (462.0 eV) is higher than RuP (461.8 eV). Both of these binding energies showed slightly oxidized Ru atoms since the binding energy shift of Ru $3p_{3/2}$ in Ru/Al_2O_3 was measured to be 461.6 eV. Similarly, the P atom in Ru_2P is more anionic than in RuP.

X-ray absorption spectroscopy experiments were also performed for the various monometallic phosphides. From the XANES results in Table S4 and Figure S7, the Mo in MoP (20,001.25 eV) and Mo_3P (20,000.61 eV) are slightly oxidized compared to the Mo-foil (20,000.00 eV) with Mo_3P being less oxidized, which agrees with the XPS measurements. The Ru K-edge absorption energy for Ru_2P was determined to be 22,117.42 eV, which is also considered oxidized compared to the reference Ru foil (22,117.2 eV). Based on these results, the Mo and Ru are electron donators in the monometallic Ru and Mo phosphides, while P acts as an electron acceptor.

As shown in Table S6, partitioning of charge density of surface atoms according to the Bader scheme reveals depletion of electronic charge density for Mo in MoP (+0.52 eV) and Mo_3P (+0.91 eV) as well as Ru in RuP (+0.11 eV) and Ru_2P (+0.13 eV). Meanwhile, the Bader charge of the P atoms were -0.52 eV, -0.91 eV, -0.11 eV, and -0.13 eV for MoP, Mo_3P, RuP, and Ru_2P. The Bader charge calculations were performed on the most dominant facet observed in XRD, which were the (101), (321), (211), and (211) for MoP, Mo_3P, RuP, and Ru_2P, respectively. These calculations also confirm the electron transfer in monometallic Ru and Mo phosphides, where Ru and Mo donate electrons to P. Taken together, XPS, XANES, and Bader charge calculations suggest that the Ru and Mo in monometallic phosphides possess Lewis acidic character (e.g., $Ru^{\delta+}$ and $Mo^{\delta+}$), which can serve as the reactant adsorption site in metal phosphides.[69]

Catalytic evaluation of bimetallic $Ru_{1.0}Mo_{1.0}P$

Our previous studies have provided evidence of catalytic enhancements with bimetallic phosphides in comparison to their monometallic counterparts.[27] Due to the high selectivity of MoP to FOL and the higher activity of RuP, we first synthesized a bimetallic $Ru_{1.0}Mo_{1.0}P$ catalyst (Table 1). The k_1, k_2, and k_3 values for $Ru_{1.0}Mo_{1.0}P$ were determined similarly to the methods described in the previous section at 100°C and 4.2 MPa H_2. The measured k_1 for $Ru_{1.0}Mo_{1.0}P$ was 0.176 h^{-1}, which was >6 times higher than the monometallic MoP, RuP, and Ru_2P. This result showcased the reaction rate improvement due to inherent bimetallic effects associated with the $Ru_{1.0}Mo_{1.0}P$ catalyst. The k_2 and k_3 values of

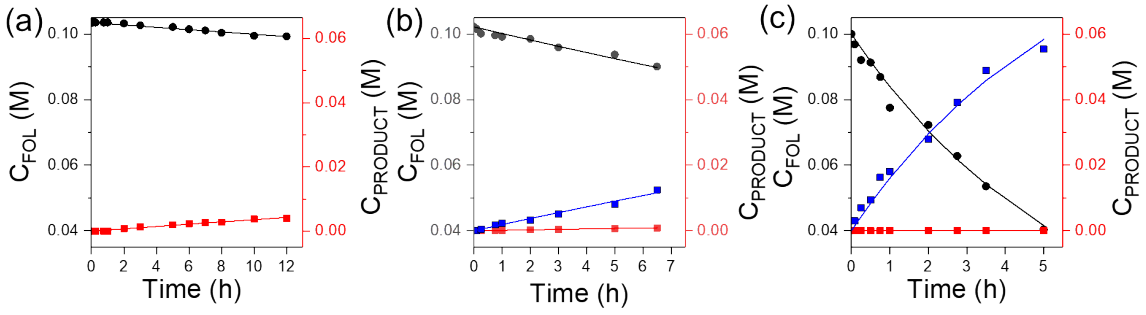

Figure 2. Concentration profiles for FOL (black filled circles), MF (red filled squares), and THFA (blue open squares) with (a) MoP, (b), RuP, and (c) Ru_2P determined experimentally (circles and squares) and fitted to the predicted reaction model (solid line).

$Ru_{1.0}Mo_{1.0}P$ were 0.0050 h^{-1} and 0.0039 h^{-1}, respectively. Although $Ru_{1.0}Mo_{1.0}P$ produced both MF and THFA, the production rates were low.

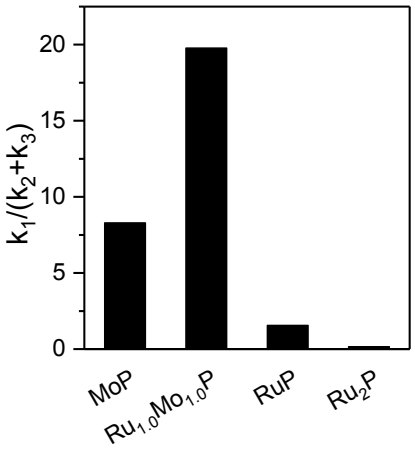

Figure 3. The ratio of $k_1/(k_2+k_3)$) for MoP, $Ru_{1.0}Mo_{1.0}P$, RuP, and Ru_2P

The highest FOL selectivity was observed with $Ru_{1.0}Mo_{1.0}P$ followed by MoP > RuP > Ru_2P, respectively. It was evident that the addition of P weakened the hydrogenation ability of Ru in the various Ru-based phosphides. Similar observations were seen in a P-doped Ru(0001) surface where the apparent charge transfer between Ru and P atoms reduced the electron back donation from Ru to the reactant.[19] Moreover, the addition of Mo shifted the hydrogenation preference from aromatics to the reduction of the carbonyl in FAL. Pairing noble metals with an oxophilic metal has been reported to create bifunctional materials capable of deoxygenating biomass-derived compounds.[70] The noble metal provides a H_2 splitting site while the oxophilic metal binds the O in the reactant.[70] Similarly, it is possible that bimetallic $Ru_{1.0}Mo_{1.0}P$ was more active compared to its monometallic counterparts due to its multifunctional behavior.

A series of experiments from ambient temperature to 150°C were performed at 4.2 MPa H_2 with $Ru_{1.0}Mo_{1.0}P$ to study the effects of temperature on the product selectivity (Figure 4). The catalyst was active as low as 20°C with 4% furfural conversion observed after 15 hr (not shown). Figure 4 depicts the selectivity and conversion variation for $Ru_{1.0}Mo_{1.0}P$ between 75°C – 125°C. At 75°C and 100°C, FOL is the dominant product with >99% selectivity. As the conversion increased to 60%, the selectivity at 100°C dropped to 97% due to the further reaction of FOL on the catalyst surface to produce MF. At 125°C the selectivity to FOL dropped from 90% at low conversion to 84% at 75% conversion. The decrease in selectivity with the increase in reaction temperature is related to the effective activation barriers for each of the reactions. However, these barriers were not extracted from additional experiments because the yields of MF were not sufficient enough to provide justification for using higher temperatures to control the reaction selectivities. However, the effective activation barrier ($E_{A,1}$) was obtained during the temperature sweep experiments for the initial reduction of FAL. The activation barrier was ~51 kJ/mol, which was similar to those reported for the commercial Cu-chromite (46 kJ/mol) and Cu/SiO_2 (50 kJ/mol).[5, 57]

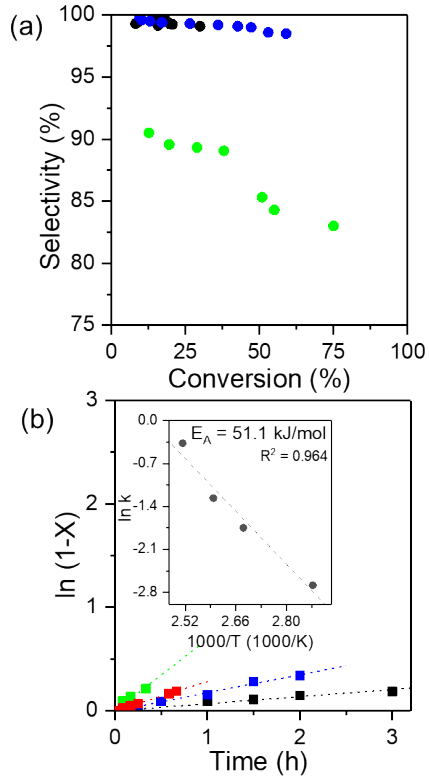

Figure 4. (a) FOL selectivity vs. conversion with $Ru_{1.0}Mo_{1.0}P$ at 75°C (blue), 100°C (black), 125°C (green), and (b) linearized rate data plotted vs. time for $Ru_{1.0}Mo_{1.0}P$ at 75°C (black – R^2 = 0.950), 100°C (blue – R^2 = 0.981), 112°C (red – R^2 = 0.910), 125°C (green – R^2 = 0.911) with an Arrhenius plot for $Ru_{1.0}Mo_{1.0}P$ (inset)

Compositional variation of bimetallic $Ru_xMo_{2-x}P$ catalysts

The kinetic studies provided evidence for catalytic enhancements with bimetallic $Ru_{1.0}Mo_{1.0}P$. Therefore, the composition of Ru, Mo, and P was varied in the solid solution to determine if the bimetallic effect could be further enhanced and to determine the potential causes for the observations. Moreover, the change in material composition influences the electronic properties of the bimetallic phosphides as shown for $Fe_xMo_{2-x}P$ ($0.8 < x < 1.5$), where the catalytic selectivity and activity for phenol hydrodeoxygenation were both influenced

by the bulk and surface compositions.[25] Therefore, in an effort to control the product selectivity, the effect of material composition in $Ru_xMo_{2-x}P$ was explored.

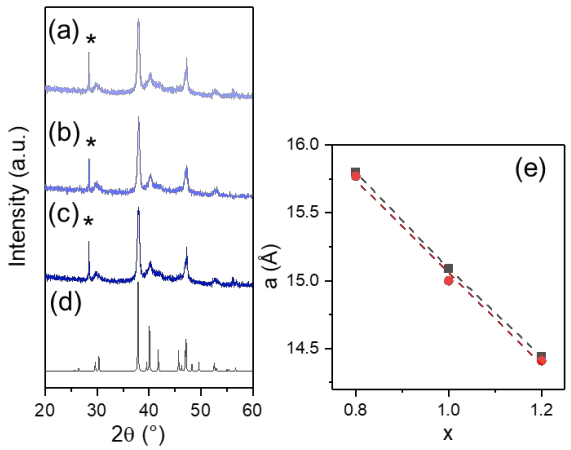

Figure 5. XRD patterns of $Ru_xMo_{2-x}P$ for (a) x = 0.8 (b) x = 1.0 (c) x = 1.2 and (d) $Ru_{1.0}Mo_{1.0}P$ reference pattern (PDF 04-015-7732). (e) The lattice parameters calculated experimentally (black) and computationally (red).

Three compositions of $Ru_xMo_{2-x}P$ were synthesized (*x* = 0.8, 1.0, and 1.2) with all of the resulting solid solutions maintaining an orthorhombic lattice. The ratio was verified using both ICP-OES and XPS (Table S2). The XRD patterns of $Ru_xMo_{2-x}P$ are presented in Figure 5. A Si (111) standard was added to each of the samples prior to the XRD measurement to eliminate peak shifts from the instrument. The Si (111) is marked with an asterisk (*) in Figure 5 and was shifted to 28.44° 2θ. Rietveld refinement was used to calculate the lattice parameter, *a*, and they were compared to the optimized, calculated lattice parameter. Figure 5e represents similarities between the experimental lattice parameter (black) and computationally calculated lattice parameter (red), which are within 1% error. The *b* and *c* cell dimensions are reported in Table S1, which are also in stong agreement.

From FAL hydrogenation experiments, the k_1 values were 0.078 h^{-1}, 0.176 h^{-1}, and 0.258 h^{-1} for $Ru_xMo_{2-x}P$ with x = 0.8, 1.0, and 1.2, respectively (Figure 6a). The catalytic performance of commercial Ru/Al_2O_3 was also analyzed to provide a comparison between a supported metal catalyst with the unsupported metal phosphides. The measured reaction rate constant for Ru/Al_2O_3 was 0.074 h^{-1}, which was 2-3 times higher than the monometallic phosphides, but it was about two times lower than bimetallic $Ru_{1.0}Mo_{1.0}P$. The FOL selectivity was not quantified due to the presence of many side products including 2-(isopropoxy)methyl furan as a result of the interaction with the solvent (isopropanol). This product was previously observed using a Ru/C catalyst for FAL hydrogenation, and it could be an intermediate to FOL production through the Meerwein-Pondorf-Verley mechanism.[62, 63]

In addition to k_1, both k_2 and k_3 were also determined by using the same method as described previously (Figure 6a). As

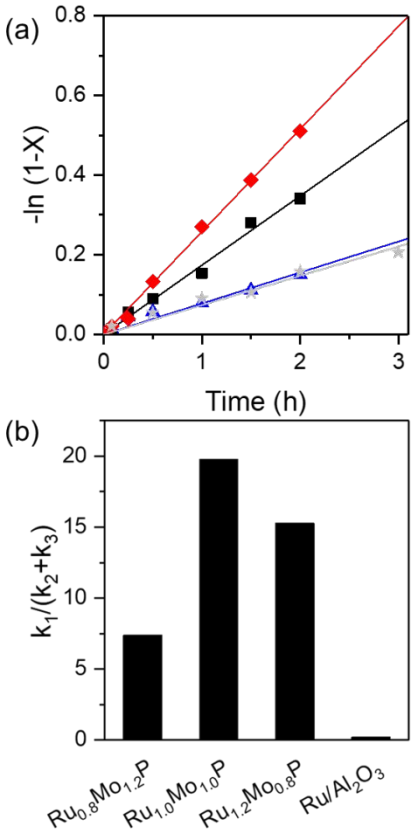

Figure 6. (a) Psuedo-1st order dependency of FAL with $Ru_xMo_{2-x}P$ where x = 0.8 (blue – R^2 = 0.964) and x = 1.0 (black – R^2 = 0.981), x = 1.2 (red – R^2 = 0.985), and 5% Ru/Al_2O_3 (grey – R^2 = 0.935) and (b) the ratio of $k_1/(k_2+k_3)$ for bimetallic $Ru_xMo_{2-x}P$ and Ru/Al_2O_3

depicted in Scheme 1, the parallel reaction pathway of FOL hydrogenation can yield both MF and THFA. However, THFA was not observed with the Mo-rich (*x* = 0.8) catalyst. Figure 7a-c shows the concentration profiles for the reactant and product species observed using $Ru_xMo_{2-x}P$ where *x* = 0.8, 1.0, and 1.2, respectively for both the measured data (circles and squares) and predicted reaction model using k-values obtained from Equations 5-7 (lines). The model provided an excellent fit to the experimental data in the time and concentration range collected. It is important to note that the FOL hydrogenation step is significantly slower with all of the catalysts compared to the first FAL hydrogenation step.

The FOL production rate constant in $Ru_xMo_{2-x}P$ was examined based on the ratio between k_1 and (k_2 + k_3). The ratio is plotted in Figure 6b with respect to x in $Ru_xMo_{2-x}P$. Although $Ru_{1.2}Mo_{0.8}P$ has the highest k_1 value, its k_2 and k_3 were higher

compared to the other bimetallic phosphides. The ratio between k_1 and $k_2 + k_3$ is the highest for $Ru_{1.0}Mo_{1.0}P$ followed by $Ru_{1.2}Mo_{0.8}P$ and $Ru_{0.8}Mo_{1.2}P$. It is possible that the high FOL selectivity is related to the metal-metal dispersion on the metal surface, which could explain why $Ru_{1.0}Mo_{1.0}P$ showed the highest FOL selectivity.[9, 10]

Theoretical and experimental surface and adsorption studies of bimetallic $Ru_xMo_{2-x}P$

XPS was used to probe the surface oxidation on the bimetallic metal phosphides (Table 2). The peak deconvolution was conducted according to the methods described in the experimental section and plotted in Figure S6. In the bimetallic RuMo phosphides, the Ru $3p_{3/2}$ was slightly negative when compared to Ru^0 at 416.6 eV. Meanwhile, the Mo was slightly positive in comparison with Mo^0 (226.8 eV). The binding energies of the phosphorus atoms were lower than P^0 (130.9 eV), suggesting anionic surface P species.[68] The XANES K-edge absorption energy of Ru and Mo are 22,116.96 eV and 20,0001.29 eV, respectively, suggesting an anionic Ru and oxidized Mo in $Ru_{1.0}Mo_{1.0}P$ similar to the XPS result. The anionic nature of Ru is in contrast with a previous report where the Ru in $Ru_{1.0}Mo_{1.0}P$ was reported positive.[69] This is due to the difference in reference point used in the data analysis, which was verified herein by using a Ru/Al_2O_3 reference rather than literature values. Overall, these observation agreed with literature reports on phosphides where charge sharing is observed in metal phosphides evident by a slightly positive species (Mo) complemented by partially negative species (Ru, P).[23, 31, 71-73] However, as shown in Table 2, the binding energy differences for the various bimetallic compositions were too small to draw strong correlations between these materials. The same observation was reported in $(Ni_{1-x}M')_2P$ (M = Cr, Fe, Co) where the binding energy shift is around 0.1 eV resolution for different Ni to M' ratio.[71]

Computational calculations were performed to determine the surface and bulk charges in the different $Ru_xMo_{2-x}P$ catalysts on the (112) surface. For comparison, additional calculations were performed on the $Ru_{1.0}Mo_{1.0}P$ (210) facet, which resulted in nearly identical Bader charges for Ru, Mo, and P (Table S5). The adsorption energies of furfural on the $Ru_{1.0}Mo_{1.0}P$ (112) and (210) facets were calculated to be -3.06 eV and -3.08 eV, respectively. These small differences would not lead to significantly different adsorption results. Therefore, the (112) facet was chosen as a representative facet for the adsorption calculations. Average partial atomic charges calculated using Bader analysis on these three catalytic surfaces are presented in Table S5. The Lewis acidic nature of $Ru_{1.0}Mo_{1.0}P$ has been probed by pyridine adsorption using diffuse reflectance infrared Fourier transform spectroscopy (DRIFTS) to show evidence of the presence of Lewis acid and no strong evidence of Brønsted acidity.[24] Since Mo is the most electron deficient atom, $Mo^{\delta+}$ is the dominant Lewis acid site in $Ru_xMo_{2-x}P$. Interestingly, the Mo atom in $Ru_{1.0}Mo_{1.0}P$ contains the highest positive charge in the bulk and on the surface.

The Bader charge for Ru in $Ru_xMo_{2-x}P$ was negative to show that Ru is an electron acceptor in the $Ru_{1.0}Mo_{1.0}P$ system (Table 2). Although the negative charge on Ru is non-intuitive, Mulliken charge analysis in $Ru_{1.0}Mo_{1.0}P$ also showed that Ru can act as an electron acceptor.[74] Moreover, similar effects have been reported in bimetallic Ce-doped Co phosphides, where the Co becomes negative with Ce addition.[75] However, caution should be applied when comparing Bader charge calculations and experimentally obtained results due to the complicated nature of the metallic states and the simplified system applied with the Bader charge calculation.[76, 77] Nevertheless, the XPS, XANES, and Bader charge analysis indicated the same electron flow from Mo to Ru and P in bimetallic $Ru_{1.0}Mo_{1.0}P$.

Computationally, the average positive partial charge on the Mo atoms on the catalytic surfaces followed the order: $Ru_{1.2}Mo_{0.8}P$ (+0.54 |e|) < $Ru_{0.8}Mo_{1.2}P$ (+0.62 |e|) < $Ru_{1.0}Mo_{1.0}P$ (+0.70 |e|), which suggested more average positive charge in $Ru_{1.0}Mo_{1.0}P$. This greater charge transfer (from Mo to Ru and P atoms) could potentially lead to stronger binding with the electron rich carbonyl O in furfural with $Ru_{1.0}Mo_{1.0}P$. It is important to note that the surface charge could also be correlated with the selectivity, where more positive charge on Mo leads to higher FOL selectivity.

Other reports have shown that the furfural orientation plays an important role in the reaction selectivity.[57, 78-82] The two binding modes that have been suggested to be most favorable in furfural adsorption are η^1(O) and η^2(C-O) (Figure S8).[57, 80] The η^1(O) surface configuration was suggested from an FTIR experiment using a Cu catalyst where the O of the carbonyl interacts with the surface to preferably produce FOL.[57] Meanwhile, the η^2(C-O) mode was suggested in group VIII

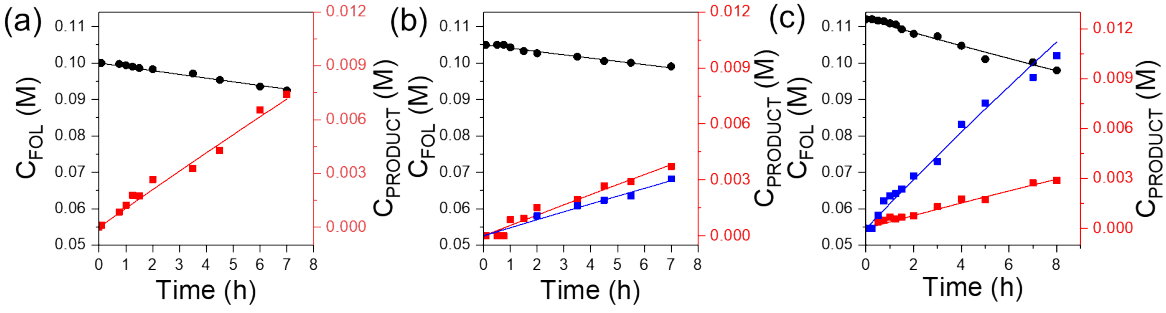

Figure 7. The concentration profiles of FOL (black), MF (red) and THFA (blue) obtained experimentally (circles and squares) and through model fits (straight line) for $Ru_xMo_{2-x}P$ where (a) x = 0.8, (b) x = 1.0, (c) x =1.2

catalysts through DFT calculations where both of the C and O from the C=O carbonyl of FAL interact with the surface leading to the formation of MF and furan.[80] The η^1(O) surface interaction was studied experimentally with DRIFTS and theoretically with DFT calculations in this work. Meanwhile the η^2(C-O) interaction was not observed,[83-85] but it was observed in other work using high resolution electron energy loss (HREEL) spectroscopy.[86] The adsorption mode was of interest as a potential descriptor for the product selectivity distribution in FAL hydrogenation. Furthermore, others have reported the incorporation of Cu into Pd decreases the amount of decarbonylation product due to the shift from η^2(C-O) in Pd to η^1(O) in Pd-Cu.[87] For the same reason, the incorporation of Mo in $Ru_xMo_{2-x}P$ may provide a FOL selectivity shift.

DRIFTS was therefore performed on the synthesized phosphide catalysts after adsorption of furfural vapor. The DRIFTS experiment was based on previous report that showed the existence of η^1(O) adsorption mode in IR spectroscopy.[57] The catalyst surface was saturated with a stream of N_2 that passed through a FAL bubbler at 200°C for 50 mins. The saturation point was indicated by the existence of two peaks at 1720 cm^{-1} from gas phase furfural C=O stretching vibration and 1670 cm^{-1} from C-O stretching band in the adsorbed FAL species as can be seen Figure S9.[57]

The adsorbed C-O vibration mode was observed at a lower wavenumber from the gas phase FAL due to a weakened C-O bond resulting from the C=O adsorption on the surface through a η^1(O)-type of interaction. This result indicated that the same carbonyl configuration in $Ru_{1.0}Mo_{1.0}P$ was observed with the Cu-catalyst. Interestingly, the adsorbed C-O vibration mode can also be observed in the DRIFTS experiments for all monometallic MoP, RuP, Ru_2P as well as bimetallic $Ru_{0.8}Mo_{1.2}P$ and $Ru_{1.2}Mo_{0.8}P$ (Figure S9) yet these catalysts have different selectivities for furfural hydrogenation. Therefore, the DRIFTS peak at ~1670 cm^{-1} could not be correlated with the selectivity with MoP, RuP, Ru_2P, $Ru_{0.8}Mo_{1.2}P$, $Ru_{1.0}Mo_{1.0}P$, and $Ru_{1.2}Mo_{0.8}P$.

DFT calculations in the gas phase were performed to benchmark the adsorption energies of FAL on the bimetallic $Ru_xMo_{2-x}P$ to the literature. The adsorption energy of *trans*-furfural (Figure 8a-c) and *cis*-furfural (Figure 8d-f) on $Ru_{0.8}Mo_{1.2}P$, $Ru_{1.0}Mo_{1.0}P$, and $Ru_{1.2}Mo_{0.8}P$ were evaluated. The adsorption energies were found to be ~0.07 – 0.31 eV higher for *trans*-furfural, which suggested more favorable adsorption of *trans*-furfural. The result was in an agreement with the previous theoretical studies.[88, 89] The center of mass (COM) was calculated for FAL and $Ru_xMo_{2-x}P$ (Table S7). Based on the DFT calculation, the COM distance to the surface was calculated to be 1.73 Å, 1.68 Å, and 3.51 Å for $Ru_{0.8}Mo_{1.2}P$, $Ru_{1.0}Mo_{1.0}P$, and $Ru_{1.2}Mo_{0.8}P$ respectively. The COM was found to be the shortest in $Ru_{1.0}Mo_{1.0}P$. Additionally, the Mo-O distance was calculated to be the shortest on $Ru_{1.0}Mo_{1.0}P$ (1.68 Å), $Ru_{0.8}Mo_{1.2}P$ (1.80 Å), and $Ru_{1.2}Mo_{0.8}P$ (1.87 Å), respectively, which suggested that the carbonyl O would preferably interact with the more oxophilic metal (i.e. Mo). The calculation also suggested that Mo-O interaction might be crucial in selective FAL hydrogenation to FOL as the shortest Mo-O distance was found in the most selective catalyst, $Ru_{1.0}Mo_{1.0}P$.

The adsorption energies for *trans*-furfural were calculated as -2.52 eV, -3.06 eV, and -2.12 eV for $Ru_{0.8}Mo_{1.2}P$, $Ru_{1.0}Mo_{1.0}P$, and $Ru_{1.2}Mo_{0.8}P$, respectively, and their corresponding binding orientation was represented in Figure 8a-c. The adsorption energy results were in a similar range with the reported furfural adsorption on supported and unsupported metal catalysts.[9, 79, 88-92] For example, the reported FAL adsorption energy on Pt(111), Pt(211), and Pt_{55} surface were -1.36 eV, -1.95 eV, and -2.52 eV respectively.[79] Similarly, the adsorption energy on Pd(111) was found to be -1.83.[89] Interestingly, the reported FAL adsorption energy on Cu(111) was in the range of -0.05 to -0.17 eV, which was significantly lower.[57] This might be due to less interaction between FAL and the surface since the tilted configuration was favored in Cu(111). It can be seen from Figure 8a-c, the FAL molecule interacted with the catalyst surface not only through the carbonyl O but also through the carbonyl C and furan ring. This type of interaction has been suggested to follow the FAL η^2(C-O) adsorption mode to produce MF.[80] Since the calculation was done in the gas phase, the DFT result was in agreement with the experimental result at higher temperature where other hydrogenation products were observed. Additionally, high MF selectivity in the gas phase reactions have been observed in other works using MoP and Ni_2P.[22, 93]

Table 2. Binding energy shift, surface, and bulk Bader charges of $Ru_xMo_{2-x}P$ on the (112) facet and binding energy shift from XPS.

	Binding energy (eV)			Surface energy (eV)			Bulk energy (eV)		
	Ru	Mo	P	Ru	Mo	P	Ru	Mo	P
$Ru_{0.8}Mo_{1.2}P$	461.5	228.2	129.0	-0.21	+0.62	-0.41	-0.15	+0.20	-0.19
$Ru_{1.0}Mo_{1.0}P$	461.5	228.2	129.1	-0.23	+0.70	-0.46	-0.18	+0.70	-0.18
$Ru_{1.2}Mo_{0.8}P$	461.4	228.1	129.2	-0.29	+0.54	-0.25	-0.13	+0.67	-0.11

ARTICLE

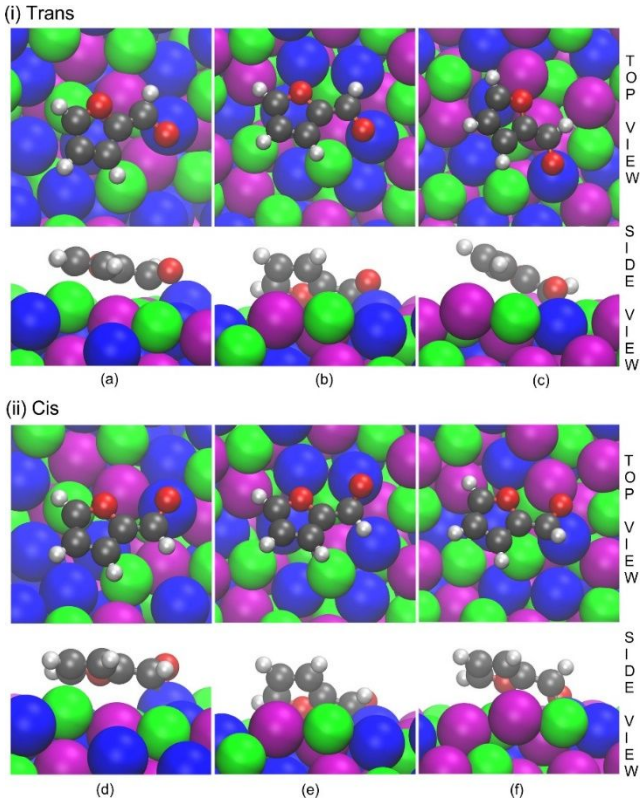

Figure 8. Adsorption of (i) trans- and (ii) cis-furfural on the (112) facets for (a) $Ru_{0.8}Mo_{1.2}P$, (b) $Ru_{1.0}Mo_{1.0}P$, and (c) $Ru_{1.2}Mo_{0.8}P$ catalyst in the horizontal mode. The atom colors are purple for Ru, blue for Mo, green for P, grey for C, silver for H, and red for O.

However, the DFT calculation could not represent the experimental result since the calculation was done in the gas phase while the reaction was performed in a condensed phase. The discrepancy could be due to the absence of other surface species in the DFT calculation such as solvents. Multiple studies have suggested solvents influenced the FAL conversion and FOL selectivity.[16, 94] Therefore, toluene and hexanes were used as solvents for FAL hydrogenation at the same reaction condition of 100°C and 4.2 MPa with 0.10 M starting concentration. According to the reaction results (Figure 9), the conversion decreased significantly in toluene and hexanes, which was consistent with previous observations. The selectivity towards FOL also decreased significantly from >99% with isopropanol to 88% in toluene and 65% in hexanes. The result showed that solvent selection can greatly influence the selectivity to FOL. As noted earlier, background experiments using isopropanol as a H_2-donor resulted in negligible conversion. The solvent effect on the surface configuration and the elucidation of reaction mechanisms are ongoing projects in our research groups.

Catalyst recyclability

Catalyst stability is one of the major problems with copper chromite, as it was reported to decrease by 40% in 4 h.[8] The deactivation has been attributed to carbonaceous formations, leaching, and sintering.[7, 8, 95-98] Therefore, a stability study was performed with $Ru_{1.0}Mo_{1.0}P$ through recycling experiments.

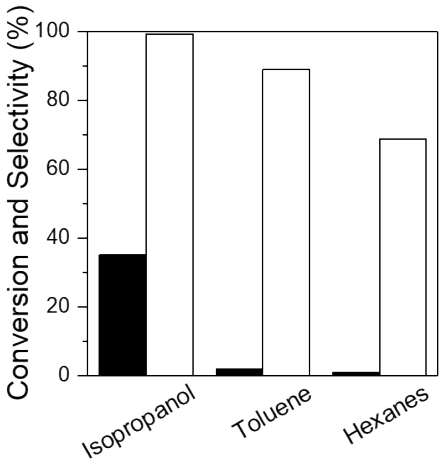

Figure 9. The effect of solvents towards FAL conversion (filled) and FOL selectivity (empty). The data were recorded after 3 h.

The stability of $Ru_{1.0}Mo_{1.0}P$ was tested with three recycling experiments. Each of the experiments was performed using 25.0 mg of catalyst for 6 hr at 100°C and 4.2 MPa. The reaction rate constant, k_1, was determined from each of the runs as well as the FAL conversion and FOL selectivity after 6 hrs. The results are presented in Figure 10. Based on the recycling experiments, the conversion at 6 h decreased slightly from 69% to 65% on the second cycle and finally to 61% on the final cycle. The reaction rate constant also decreased from 0.176 h^{-1} on the first cycle to 0.171 h^{-1} and 0.165 h^{-1} for the second and third cycle, respectively. Meanwhile the selectivity towards FOL remained high at >97% for all cycles. The deactivation seen from each cycle could be due to surface oxidation during a drying step between the cycles. To overcome this issue, re-reduction at 650°C for 2 h under 160 mL/min of H_2 was conducted on the materials recovered from the third cycle. The re-reduced material was then tested at the same reaction

condition by loading the same catalyst weight. In the fourth cycle, the conversion was recovered back to 71% with a selectivity of 96%.

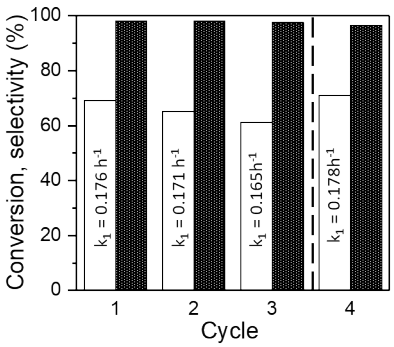

Figure 10. Conversion (empty) and FOL selectivity (shaded) of $Ru_{1.0}Mo_{1.0}P$ for FAL hydrogenation at 4.2 MPa and 100°C in recycling experiment. The dotted line signifies re-reduction.

Conclusions

The hydrogenation of FAL was successfully demonstrated over a series of monometallic phosphides (MoP, RuP, Ru_2P) and bimetallic phosphides ($Ru_xMo_{2-x}P$ for x = 0.8, 1.0, and 1.2). Bimetallic $Ru_{1.0}Mo_{1.0P}$ and monometallic MoP exhibited high selectivity (99%) towards FOL production in FAL hydrogenation with minimal production of MF. The catalytic results also showed that a bimetallic effect was observed through an increase in the reaction rate of furfural with bimetallic $Ru_xMo_{2-x}P$ compared to its monometallic analogues. Kinetic evaluation determined an activation energy (E_A) of 51.1 kJ/mol for $Ru_{1.0}Mo_{1.0}P$, which was comparable to Cu-based catalysts reported in the literature. The ratio between k_1/k_2+k_3 was found to be the highest with $Ru_{1.0}Mo_{1.0}P$ > $Ru_{1.2}Mo_{0.8}P$ > MoP > $Ru_{0.8}Mo_{1.2}P$ > RuP > Ru_2P, which suggested that the production of FOL per reaction rate was more favored with $Ru_{1.0}Mo_{1.0}P$. DFT calculations in the gas phase showed the most favorable adsorption on $Ru_{1.0}Mo_{1.0}P$ > $Ru_{0.8}Mo_{1.2}P$ > $Ru_{1.2}Mo_{0.8}P$ which was consistent with the FOL selectivity trend. Additionally, the use of isopropanol was found to positively influence the selectivity to FOL, while non-polar solvents (toluene and hexanes) decreased the conversion and selectivity. Lastly, we have shown that $Ru_{1.0}Mo_{1.0}P$ can be recovered to its original rate through re-reduction. Overall, this study provides strong support for the use of bimetallic phosphides for furfural hydrogenation to furfuryl alcohol as well as other selective hydrogenation reactions.

Conflicts of interest

There are no conflicts to declare

Acknowledgements

This work was supported in part by funding from the National Science Foundation through the CAREER award program (CBET-1351609 and CBET- 1752036), Defense University Research Instrumentation Program under AFOSR Award No. FA9550-17-1-0376, Patrick and Jana Eilers Fellowship from ND Energy, and Center of Environmental Science and Technology (CEST) Fellowship. We thank CEST for the use ICP-OES and Material Characterization Facility (MCF) at the University of Notre Dame for the use of XRD and XPS. The computation portion of this work used resources at the High Performance Computing Collaboratory and the National Energy Research Scientific Computing Center (NERSC), a U.S. Department of Energy Office of Science User Facility operated under Contract No. DE-AC02-05CH11231 at the Mississippi State University. We acknowledge VESTA,[93] CANVAS, and VMD for use of their software to create images of the crystal structures contained in this manuscript. The XANES portion of the work used resources from U.S. Department of Energy (DOE) Office of Science User Facility operated for the DOE Office of Science by Argonne National Laboratory under contract No. DE-AC02-06CH11357. We thank Dr. Ce Yang and Prof. Jeffrey T. Miller at Purdue University, as well as Dr. Hui Li and Prof. Christopher Paolucci at University of Notre Dame for assistance at the beamline.

Notes and references

1. X. D. Li, P. Jia and T. F. Wang, *ACS Catal.*, 2016, **6**, 7621-7640.
2. J. C. Serrano-Ruiz, R. Luque and A. Sepulveda-Escribano, *Chem. Soc. Rev.*, 2011, **40**, 5266-5281.
3. R. Mariscal, P. Maireles-Torres, M. Ojeda, I. Sadaba and M. L. Granados, *Energ. Environ. Sci.*, 2016, **9**, 1144-1189.
4. K. Bauer, J. Panten and H. Surburg, *Common fragrance and flavor materials : preparation, properties and uses*, Weinheim : Wiley-VCH, 2016.
5. R. Rao, A. Dandekar, R. T. K. Baker and M. A. Vannice, *J. Catal.*, 1997, **171**, 406-419.
6. R. Connor, K. Folkers and H. Adkins, *J. Am. Chem. Soc.*, 1931, **53**, 2012-2012.
7. H. B. Zhang, Y. Lei, A. J. Kropf, G. H. Zhang, J. W. Elam, J. T. Miller, F. Sollberger, F. Ribeiro, M. C. Akatay, E. A. Stach, J. A. Dumesic and C. L. Marshall, *J. Catal.*, 2014, **317**, 284-292.
8. D. X. Liu, D. Zemlyanov, T. P. Wu, R. J. Lobo-Lapidus, J. A. Dumesic, J. T. Miller and C. L. Marshall, *J. Catal.*, 2013, **299**, 336-345.
9. B. Seemala, C. M. Cai, R. Kumar, C. E. Wyman and P. Christopher, *ACS Sustain. Chem. Eng.*, 2018, **6**, 2152-2161.
10. H. Sheng and R. F. Lobo, *Chemcatchem*, 2016, **8**, 3402-3408.
11. S. Srivastava, G. C. Jadeja and J. Parikh, *Chem. Eng. Res. Des.*, 2018, **132**, 313-324.
12. S. Srivastava, N. Solanki, P. Mohanty, K. A. Shah, J. K. Parikh and A. K. Dalai, *Catal. Lett.*, 2015, **145**, 816-823.
13. C. P. Jimenez-Gomez, J. A. Cecilia, D. Duran-Martin, R. Moreno-Tost, J. Santamaria-Gonzalez, J. Merida-Robles, R.

Mariscal and P. Maireles-Torres, *J. Catal.*, 2016, **336**, 107-115.
14. K. Yan and A. C. Chen, *Fuel*, 2014, **115**, 101-108.
15. N. Merat, C. Godawa and A. Gaset, *J Chem Technol Biot*, 1990, **48**, 145-159.
16. A. B. Merlo, V. Vetere, J. F. Ruggera and M. L. Casella, *Catal. Commun.*, 2009, **10**, 1665-1669.
17. J. J. Musci, A. B. Merlo and M. L. Casella, *Catal. Today*, 2017, **296**, 43-50.
18. A. O'Driscoll, T. Curtin, W. Y. Hernandez, P. Van Der Voort and J. J. Leahy, *Org. Process Res. Dev.*, 2016, **20**, 1917-1929.
19. A. Sampath, S. A. Chang and D. W. Flaherty, *J. Phys. Chem. C*, 2018, **122**, 23600-23609.
20. S. E. Habas, F. G. Baddour, D. A. Ruddy, C. P. Nash, J. Wang, M. Pan, J. E. Hensley and J. A. Schaidle, *Chem. Mater.*, 2015, **27**, 7580-7592.
21. R. H. Bowker, M. C. Smith, M. L. Pease, K. M. Slenkamp, L. Kovarik and M. E. Bussell, *ACS Catal.*, 2011, **1**, 917-922.
22. C. P. Jiménez-Gómez, J. A. Cecilia, R. Moreno-Tost and P. Maireles-Torres, *Chemcatchem*, 2017, **9**, 2881-2889.
23. Y. Bonita and J. C. Hicks, *J. Phys. Chem. C*, 2018, **122**, 13322-13332.
24. Y. Bonita, T. P. O'Connell, H. E. Miller and J. C. Hicks, *Ind. Eng. Chem. Res.*, 2019, **58**, 3650-3658.
25. D. J. Rensel, J. Kim, V. Jain, Y. Bonita, N. Rai and J. C. Hicks, *Catal. Sci. Technol.*, 2017, **7**, 1857-1867.
26. D. J. Rensel, J. Kim, Y. Bonita and J. C. Hicks, *Appl. Catal. A*, 2016, **524**, 85-93.
27. D. J. Rensel, S. Rouvimov, M. E. Gin and J. C. Hicks, *J. Catal.*, 2013, **305**, 256-263.
28. G. Corro and R. Gomez, *React. Kinet. Catal. Lett.*, 1979, **12**, 145-150.
29. S. Doniach and M. Sunjic, *J. Phys. C*, 1970, **3**, 285-&.
30. D. J. Morgan, *Surf. Interface Anal.*, 2015, **47**, 1072-1079.
31. P. E. R. Blanchard, A. P. Grosvenor, R. G. Cavell and A. Mar, *Chem. Mater.*, 2008, **20**, 7081-7088.
32. A. D. Becke, *J. Chem. Phys.*, 2014, **140**.
33. R. G. Parr, *Horizons of Quantum Chemistry*, 1980, 5-15.
34. G. Kresse and J. Hafner, *Phys. Rev. B.*, 1993, **47**, 558-561.
35. G. Kresse and J. Hafner, *Phys. Rev. B.*, 1994, **49**, 14251-14269.
36. G. Kresse and J. Furthmüller, *Phys. Rev. B.*, 1996, **54**, 11169-11186.
37. G. Kresse and J. Furthmüller, *Comput. Mater. Sci.*, 1996, **6**, 15-50.
38. J. Klimeš, D. R. Bowler and A. Michaelides, *Phys. Rev. B.*, 2011, **83**.
39. J. Klimeš, D. R. Bowler and A. Michaelides, *J. Phys.-Condens. Mat.*, 2009, **22**, 022201.
40. P. E. Blöchl, *Phys. Rev. B.*, 1994, **50**, 17953-17979.
41. G. Kresse and D. Joubert, *Phys. Rev. B.*, 1999, **59**, 1758-1775.
42. P. J. Stephens, F. J. Devlin, C. F. Chabalowski and M. J. Frisch, *J. Phys. Chem.*, 1994, **98**, 11623-11627.
43. M. Methfessel and A. T. Paxton, *Phys. Rev. B.*, 1989, **40**, 3616-3621.
44. A. Genova and M. Pavanello, *J. Phys.-Condens. Mat.*, 2015, **27**.
45. G. Henkelman, A. Arnaldsson and H. Jónsson, *Comput. Mater. Sci.*, 2006, **36**, 354-360.
46. M. Yu and D. R. Trinkle, *J. Chem. Phys.*, 2011, **134**, 064111.
47. W. Tang, E. Sanville and G. Henkelman, *J. Phys.-Condens. Mat.*, 2009, **21**, 084204.
48. E. Sanville, S. D. Kenny, R. Smith and G. Henkelman, *J. Comput. Chem.*, 2007, **28**, 899-908.
49. C. Stinner, R. Prins and T. Weber, *J. Catal.*, 2000, **191**, 438-444.
50. V. M. L. Whiffen and K. J. Smith, *Energ. Fuel*, 2010, **24**, 4728-4737.
51. R. Wang and K. J. Smith, *Catal. Lett.*, 2014, **144**, 1594-1601.
52. V. M. L. Whiffen, K. J. Smith and S. K. Straus, *Appl. Catal. A*, 2012, **419**, 111-125.
53. S. T. Oyama, *J. Catal.*, 2003, **216**, 343-352.
54. S. J. Sawhill, K. A. Layman, D. R. Van Wyk, M. H. Engelhard, C. Wang and M. E. Bussell, *J. Catal.*, 2005, **231**, 300-313.
55. P. D. Vaidya and V. V. Mahajani, *Ind. Eng. Chem. Res.*, 2003, **42**, 3881-3885.
56. R. S. Rao, R. T. K. Baker and M. A. Vannice, *Catal. Lett.*, 1999, **60**, 51-57.
57. S. Sitthisa, T. Sooknoi, Y. G. Ma, P. B. Balbuena and D. E. Resasco, *J. Catal.*, 2011, **277**, 1-13.
58. S. H. Pang and J. W. Medlin, *ACS Catal.*, 2011, **1**, 1272-1283.
59. R. B. Dean and W. J. Dixon, *Anal. Chem.*, 1951, **23**, 636-638.
60. S. Jaatinen, J. Touronen, R. Karinen, P. Uusi-Kyyny and V. Alopaeus, *J. Chem. Thermodyn.*, 2017, **112**, 1-6.
61. P. Xiao, M. A. Sk, L. Thia, X. M. Ge, R. J. Lim, J. Y. Wang, K. H. Lim and X. Wang, *Energ. Environ. Sci.*, 2014, **7**, 2624-2629.
62. P. Panagiotopoulou and D. G. Vlachos, *Appl. Catal. A*, 2014, **480**, 17-24.
63. M. Koehle and R. F. Lobo, *Catal. Sci. Technol.*, 2016, **6**, 3018-3026.
64. J. Luo, J. Yu, R. J. Gorte, E. Mahmoud, D. G. Vlachos and M. A. Smith, *Catal. Sci. Technol.*, 2014, **4**, 3074-3081.
65. M. A. Tike and V. V. Mahajani, *Ind. Eng. Chem. Res.*, 2007, **46**, 3275-3282.
66. Y. Song, W. Li, M. Zhang and K. Tao, *Front. Chem. Sci. Eng.*, 2007, **1**, 151-154.
67. S. Carenco, D. Portehault, C. Boissiere, N. Mezailles and C. Sanchez, *Chem. Rev.*, 2013, **113**, 7981-8065.
68. M. Pelavin, D. N. Hendrickson, J. M. Hollander and W. L. Jolly, *J. Phys. Chem.*, 1970, **74**.
69. V. Jain, Y. Bonita, A. Brown, A. Taconi, J. C. Hicks and N. Rai, *Catal. Sci. Technol.*, 2018, **8**, 4083-4096.
70. A. M. Robinson, J. E. Hensley and J. W. Medlin, *ACS Catal.*, 2016, **6**, 5026-5043.
71. P. E. R. Blanchard, A. P. Grosvenor, R. G. Cavell and A. Mar, *J. Mater. Chem.*, 2009, **19**, 6015-6022.
72. A. P. Grosvenor, R. G. Cavell and A. Mar, *J. Solid State. Chem.*, 2007, **180**, 2702-2712.
73. A. P. Grosvenor, S. D. Wik, R. G. Cavell and A. Mar, *Inorg. Chem.*, 2005, **44**, 8988-8998.
74. W. Wong-Ng, W. Y. Ching, Y.-N. Xu, J. A. Kaduk, I. Shirotani and L. Swartzendruber, *Phys. Rev. B.*, 2003, **67**, 144523.
75. W. Gao, M. Yan, H.-Y. Cheung, Z. Xia, X. Zhou, Y. Qin, C.-Y. Wong, J. C. Ho, C.-R. Chang and Y. Qu, *Nano Energy*, 2017, **38**, 290-296.
76. A. Walsh, A. A. Sokol, J. Buckeridge, D. O. Scanlon and C. R. A. Catlow, *J. Phys. Chem. Lett.*, 2017, **8**, 2074-2075.

77. A. Walsh, A. A. Sokol, J. Buckeridge, D. O. Scanlon and C. R. A. Catlow, *Nat. Mater.*, 2018, **17**, 958-964.
78. S. H. Pang, C. A. Schoenbaum, D. K. Schwartz and J. W. Medlin, *Nat. Commun.*, 2013, **4**.
79. Q. X. Cai, J. G. Wang, Y. G. Wang and D. H. Mei, *Aiche J.*, 2015, **61**, 3812-3824.
80. S. Sitthisa, W. An and D. E. Resasco, *J. Catal.*, 2011, **284**, 90-101.
81. S. Sitthisa and D. E. Resasco, *Catal. Lett.*, 2011, **141**, 784-791.
82. M.-d. Qian, J.-l. Xue, S.-j. Xia, Z.-m. Ni, J.-h. Jiang and Y.-y. Cao, *J. Fuel Chem. Technol.*, 2017, **45**, 34-42.
83. R. G. Greenler, D. R. Snider, D. Witt and R. S. Sorbello, *Surf. Sci.*, 1982, **118**, 415-428.
84. R. G. Greenler, *J. Chem. Phys.*, 1966, **44**, 310-315.
85. H. A. Pearce and N. Sheppard, *Surf. Sci.*, 1976, **59**, 205-217.
86. J. L. Davis and M. A. Barteau, *Surf. Sci.*, 1990, **235**, 235-248.
87. S. Sitthisa, T. Pham, T. Prasomsri, T. Sooknoi, R. G. Mallinson and D. E. Resasco, *J. Catal.*, 2011, **280**, 17-27.
88. Y. Shi, Y. L. Zhu, Y. Yang, Y. W. Li and H. J. Jiao, *ACS Catal.*, 2015, **5**, 4020-4032.
89. B. Liu, L. Cheng, L. Curtiss and J. Greeley, *Surf. Sci.*, 2014, **622**, 51-59.
90. S. Wang, V. Vorotnikov, J. E. Sutton and D. G. Vlachos, *ACS Catal.*, 2014, **4**, 604-612.
91. V. Vorotnikov, G. Mpourmpakis and D. G. Vlachos, *ACS Catal.*, 2012, **2**, 2496-2504.
92. W. Wan, G. R. Jenness, K. Xiong, D. G. Vlachos and J. G. Chen, *Chemcatchem*, 2017, **9**, 1701-1707.
93. Y. Z. Wang, F. Liu, H. Han, L. F. Xiao and W. Wu, *Chemistryselect*, 2018, **3**, 7926-7933.
94. X. Chen, L. Zhang, B. Zhang, X. Guo and X. Mu, *Sci. Rep.*, 2016, **6**, 28558.
95. B. J. O'Neill, D. H. K. Jackson, A. J. Crisci, C. A. Farberow, F. Y. Shi, A. C. Alba-Rubio, J. L. Lu, P. J. Dietrich, X. K. Gu, C. L. Marshall, P. C. Stair, J. W. Elam, J. T. Miller, F. H. Ribeiro, P. M. Voyles, J. Greeley, M. Mavrikakis, S. L. Scott, T. F. Kuech and J. A. Dumesic, *Angew. Chem. Int. Edit.*, 2013, **52**, 13808-13812.
96. M. V. Twigg and M. S. Spencer, *Appl. Catal. A*, 2001, **212**, 161-174.
97. J. G. M. Bremner and R. K. F. Keeys, *J. Chem. Soc.*, 1947, DOI: DOI 10.1039/jr9470001068, 1068-1080.
98. G. Seo and H. Chon, *J. Catal.*, 1981, **67**, 424-429.

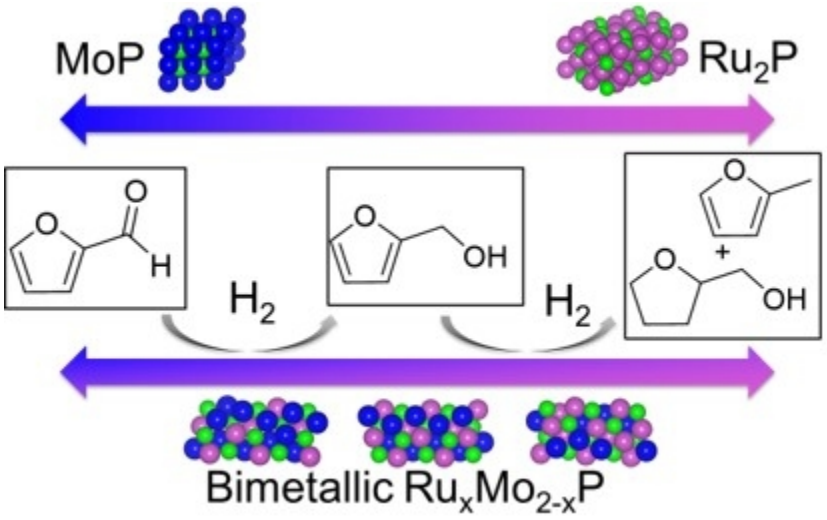

70x45mm (149 x 149 DPI)